Computers in Biology and Medicine 120 (2020) 103701

Contents lists available at ScienceDirect

Computers in Biology and Medicine

journal homepage: http://www.elsevier.com/locate/compbiomed

Development of a new fully three-dimensional methodology for tumours delineation in functional images

Albert Comelli [a], Samuel Bignardi [b], Alessandro Stefano [c,*], Giorgio Russo [c,d], Maria Gabriella Sabini [d], Massimo Ippolito [e], Anthony Yezzi [b]

[a] Ri.MED Foundation, via Bandiera 11, 90133, Palermo, Italy
[b] Department of Electrical and Computer Engineering, Georgia Institute of Technology, Atlanta, GA, 30332, USA
[c] Institute of Molecular Bioimaging and Physiology, National Research Council (IBFM-CNR), Cefalù, Italy
[d] Medical Physics Unit, Cannizzaro Hospital, Catania, Italy
[e] Nuclear Medicine Department, Cannizzaro Hospital, Catania, Italy

ARTICLE INFO

Keywords:
Cancer
Active surface
PET imaging
Metabolic tumour volume
3D segmentation

ABSTRACT

Delineation of tumours in Positron Emission Tomography (PET) plays a crucial role in accurate diagnosis and radiotherapy treatment planning. In this context, it is of outmost importance to devise efficient and operator-independent segmentation algorithms capable of reconstructing the tumour three-dimensional (3D) shape. In previous work, we proposed a system for 3D tumour delineation on PET data (expressed in terms of Standardized Uptake Value - SUV), based on a two-step approach. Step 1 identified the slice enclosing the maximum SUV and generated a rough contour surrounding it. Such contour was then used to initialize step 2, where the 3D shape of the tumour was obtained by separately segmenting 2D PET slices, leveraging the slice-by-slice marching approach. Additionally, we combined active contours and machine learning components to improve performance. Despite its success, the slice marching approach poses unnecessary limitations that are naturally removed by performing the segmentation directly in 3D. In this paper, we migrate our system into 3D. In particular, the segmentation in step 2 is now performed by evolving an active surface directly in the 3D space. The key points of such an advancement are that it performs the shape reconstruction on the whole stack of slices simultaneously, naturally leveraging cross-slice information that could not be exploited before. Additionally, it does not require any specific stopping condition, as the active surface naturally reaches a stable topology once convergence is achieved.

Performance of this fully 3D approach is evaluated on the same dataset discussed in our previous work, which comprises fifty PET scans of lung, head and neck, and brain tumours. The results have confirmed that a benefit is indeed achieved in practice for all investigated anatomical districts, both quantitatively, through a set of commonly used quality indicators (dice similarity coefficient >87.66%, Hausdorff distance < 1.48 voxel and Mahalanobis distance < 0.82 voxel), and qualitatively in terms of Likert score (>3 in 54% of the tumours).

1. Introduction

Positron Emission Tomography (PET) has become increasingly popular in cancer studies, even though PET images typically present lower spatial resolution and pose several additional complications (e.g. the partial volume effect [1]) when compared to other popular imaging approaches such as Magnetic Resonance Imaging (MRI) and Computed Tomography (CT). The main reason for this popularity is that functional indexes derived from PET imaging, for example the Standardized Uptake Value (SUV, i.e. the ratio between tissue radioactivity concentration and the injected dose normalized by the body weight), can be predictive of the patient's oncological outcome and are useful in obtaining an objective evaluation of patient response to treatment [2]. This makes PET imaging a suitable tool in clinical cancer treatment decision making [3–5]. In addition, PET imaging is a crucial step towards precise radiation therapy treatment planning. In the era of "dose painting" [6], PET images are used to identify the most aggressive areas within the tumour. Indeed, the inclusion of PET in radiotherapy planning conveys valuable

* Corresponding author.
E-mail address: alessandro.stefano@ibfm.cnr.it (A. Stefano).

https://doi.org/10.1016/j.compbiomed.2020.103701
Received 13 December 2019; Received in revised form 11 March 2020; Accepted 11 March 2020
Available online 16 March 2020

guidance for targeting tumours more efficiently, escalating the radiation dose [7,8]. Additionally, texture information from PET imaging is being investigated in several recent radiomics studies [9–11]. On the one hand, such applications depend on a reliable metabolic tumour volume (MTV) segmentation strategy as a necessary prerequisite for obtaining accurate and reproducible evaluations of the PET parameters associated to the anomalous tissue [12]. On the other hand, due to the low spatial resolution of PET images caused by detector crystal size, scanner geometry, and positron range [1,13], delineating the metabolic volume of the tumour is still considered challenging and no general agreement has reached concerning which segmentation approach performs best [14]. Manual contouring is still a common choice in clinical practice. Unfortunately, it is very time-consuming and results tend to vary according to expertise and clinical specialization of the operator.

Concerning the computer-aided segmentation, several automatic or semi-automatic algorithms have been proposed so far [15,16] also in other image techniques and application fields such as cardiac and cerebral districts [17,18]. In the following, a brief overview is given, focusing on PET imaging. Fixed, adaptive and iterative thresholding-based [15,19] and region growing methods [20] are the most common. Nevertheless, due to the image noise and scanner type, these methods typically fail when delineating heterogeneous tumours [15]. Stochastic methods [21] show high accuracy in the heterogeneous tumour delineation outperforming thresholding methods taking advantage of the fuzziness of lesion boundaries in PET images. Among classification and clustering methods, Fuzzy C-Means (FCM) [22] is the most used but it is not suited for multi-focal region segmentation [23]. Affinity propagation may be used, in principle, to partition an image according to an optimal threshold obtained by investigating the image's histogram, but so far it has been successful only on rabbit images [24]. Graph-based methods, such as graph cut and random walk [25,26], have been applied to functional image contouring as well. Their major drawback is the "min cuts" effect that occurs when a small set of seeds is used. Recently, Conventional Neural Networks (CNN) have been successfully applied for the segmentation of lung and head-and-neck tumours [14]. Unfortunately however, their application is still computationally challenging and require big datasets for training. For completeness, it is worth to mention that hybrid approaches, which perform the segmentation on PET and CT (or MRI) simultaneously, have been proposed as well [28–31]. Nevertheless, in this paper we shall not discuss such a class of applications.

Among the most efficient segmentation algorithms, active contours (AC) [27–30] leverage a silhouette initially placed around the tumour, which deforms and moves to fit the tumour boundaries. Such iterative evolution of the contour is obtained by minimizing the so-called "energy", a real-valued multi-parameter function. The lower the energy, the better the segmentation. In the past, a combination of active contour and anisotropic diffusion filtering, followed by a multi-resolution contourlet transform has been proposed in Ref. [31]. The main limitation of this algorithm is a heavy dependence on user-defined parameters. Another solution included histogram fuzzy C-means clustering and textural information to constrain the active contour [32]. Nevertheless, it suffers when a local high uptake area sits very close to the contour and is influenced by the choice of the initial region of interest (ROI).

In our recent studies [33–35], we investigated the use of the 18F-fluoro-2-deoxy-*d*-glucose (FDG) and the 11C-labeled Methionine (MET) radiotracers in PET and we devised an algorithm for the semi-automatic tumour segmentation in PET-SUV imaging that became fully automatic in the case of brain lesions [36,37]. In detail, Comelli et al. [33] introduced a semi-automatic segmentation performed in two steps (Fig. 1-A).

In both steps, PET slices were travelled upward and downward starting from a specific initial slice. In step 1, the manual segmentation on a slice chosen by the user was propagated and adapted to successive slices using the region growing algorithm to identify the slice enclosing the maximum SUV and generate a rough contour surrounding it. Such contour was then used to initialize step 2, where slices were travelled once more and the segmentation was performed leveraging an active contour. Step 2, in the specific, leveraged a slice-by-slice marching algorithm coupled with a suitable stopping condition, while segmentation on single slices was achieved through AC. In two subsequent papers [34,35], we proposed a very innovative idea: we coupled the active contour with machine learning (ML) components to take into account tissue classification. Despite combining ML approaches and active contour may seem to have been considered by many authors, most approaches have kept active contour and ML as independent entities. In contrast, we

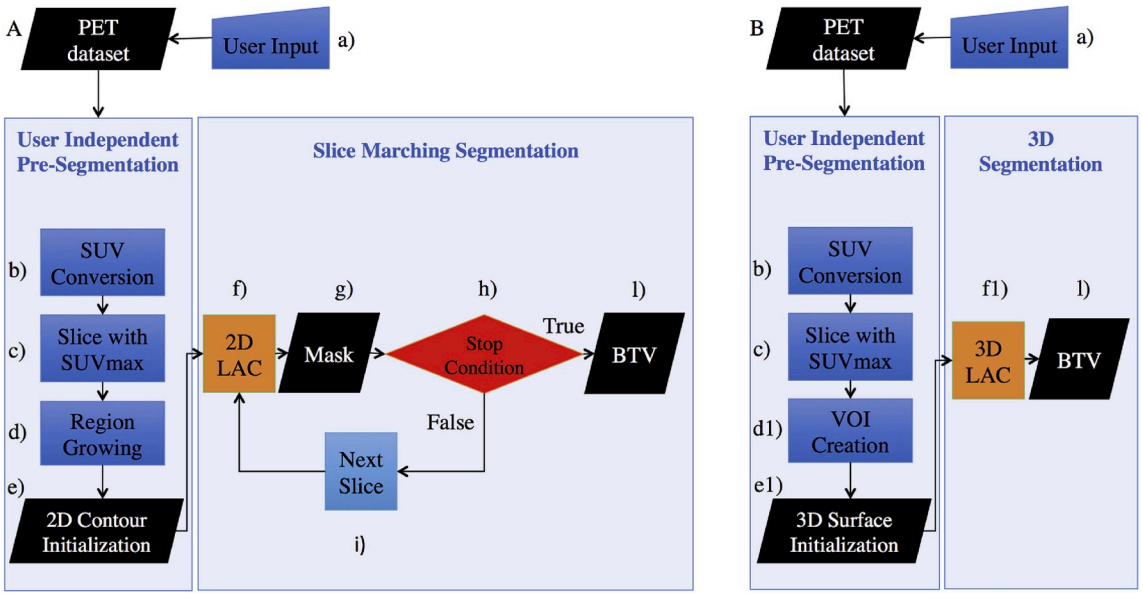

Fig. 1. A comparison of the two-step PET segmentation algorithm from our previous work (A) and the new implementation introduced here (B). In step 2 (the right block), the new implementation substitutes the slice-wise (i.e. 2D) active contour and the slice-by-slice marching approach (blocks f, g, h, and i, in figure A) with a fully 3D shape evolution (block f1, figure B). In this way, cross-slice information that was previously overlooked is now fully leveraged. Further, the shape evolution can run to convergence (i.e. to a stable shape) without the need of an artificial stopping condition. Additionally, the User-independent Pre-Segmentation (step 1, block e) was modified to provide a 3D shape as initialization to step 2.

included tissue classification directly within the active contour framework by modifying the mathematical formulation of the energy to be minimized.

Since the main motivation to our previous work was to devise an algorithm capable of satisfying the increasing need for efficient, repeatable and real-time PET segmentations; the slice-by-slice marching approach represented a very convenient and efficient simplification.

While the previous algorithm moved an important step toward 3D segmentation, it might be argued that, since the distance of PET slices is greater compared to the pixel size, the planar resolution is greater than the vertical resolution, resulting in the introduction of an artificial preferential direction. Additionally, even starting with a boundary inherited from an adjacent slice, the 2D evolution of the contour on the slice does not entirely consider what is actually happening in the slices above and below. Marching through slices is efficient as long as the tumour's cross-section changes continuously between slices. While the distance between slices is short enough to guarantee that a shape misidentification is unlikely, one could nevertheless conceive three-dimensional tumour shapes capable of generating topologically disconnected entities on the PET slice. Fig. 2 conceptually illustrates this issue. It is worthy of note that the same shape would be correctly retrieved if the marching direction was reversed.

In other words, the choice of using the slice marching approach poses unnecessary limitations that are naturally removed by solving the segmentation directly in 3D. Reformulating [33–35] in a fully 3D framework requires three components (with reference to Fig. 1):

1. Modify block 1: (e) becomes (e1), where a 3D initialization is generated
2. Replacing the slice-marching active contour with the evolution of a surface embedded in the 3D data volume, i.e. an active surface.
3. Reformulate the energy functional described in Ref. [34,35] to work efficiently in 3D.

Since point 3 is the most involved, one may wonder (as we did ourselves) if the exercise of extending the whole machinery described in Ref. [33] (i.e. even without considering tissue classification) into 3D, pays off by actually improving segmentation in practice.

Therefore, we propose a reconstruction based on the evolution of a three-dimensional active surface (i.e. truly 3D). Similarly to our previous investigation, to include the functional aspects of the tumour, PET data are converted into SUV before the segmentation. In the present study, however, the contribution of the tissue classification to the segmentation process [34,35] will not be discussed, as it is not yet included in the current version of the algorithm. The latter will be investigated in a forthcoming paper. Summarizing, the key contributions of the present paper are: 1) to provide discussion on the points 1 and 2 introduced earlier, 2) remove unnecessary limitations of our previous work, 3) evaluate whether the migration from the slice-marching approach into 3D yields a practical benefit in terms of segmentation performance (in absence of tissue classification), and consequently 4) motivate the effort of developing and embedding a full 3D classification into the active surface energy. Evaluation of the performance is obtained by comparing the gold standards, provided by three M.D., and the contours corresponding to the intersection of the active surface with the PET slices. The results obtained on a dataset which includes fifty clinical cases and comprises tumours in lung, head and neck, and brain districts, confirm the effectiveness of the adopted methodology.

In the following: section 2 describes the new full 3D approach, section 3 introduces the PET dataset, and section 4 describes the performance of the proposed method. Finally, Sections 5 and 6 are devoted to discussion and conclusions, respectively.

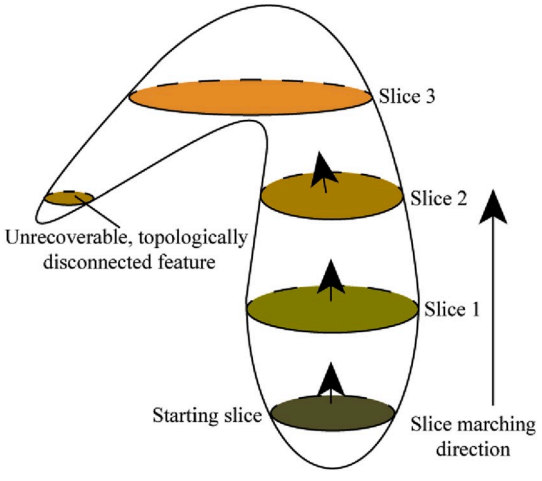

Fig. 2. Example of a three-dimensional tumour shape that, once sliced, introduces topologically disjoint features that potentially, could not be captured by the slice-marching approach. The disconnected cross-section on the left is not a continuous transformation of the contour being propagated from slice 1 and may remain undetected. Note that the same shape would be correctly reconstructed by reversing the marching direction. Such topological changes between slices are naturally accommodated by the active surface.

2. Overview of the proposed method

The present algorithm inherits several features from the system described in our previous work [33]. For clarity sake, we will briefly summarize the main characteristics of such a system (Fig. 1-A), then highlighting the key novelty aspects introduced (Fig. 1-B). In Fig. 1-A, the first block (grouping steps b to e) consists of a pre-segmentation in which the user roughly identifies the area containing the cancer on just a single PET slice. The algorithm then computes (using the region growing method) a user-independent ROI and automatically finds an optimal starting mask. By optimal starting mask, we mean a 2D contour sitting at an optimal location, in terms of slice position and rough shape. Such a mask may actually lay on a slice different from the one initially highlighted by the operator. By construction, both the ROI and the optimal mask still belong to the same anatomical anomaly and encircle the highest radiotracer uptake area (SUV_{max}). Details can be found in Ref. [33].

Once this operation is concluded, the optimal initial mask is feed to the next block of the system, where the segmentation is performed using a local region-based active contour. Here, the algorithm performs the fine segmentation using a slice-by-slice marching approach which starts at the slice containing the initial mask and propagates upward and downward. Every time a slice has segmented, the contour is propagated to the next adjacent slice until the stopping criterion is met. The final 3D shape corresponds to the assembly of all the contours produced on every slice.

The present algorithm (Fig. 1-B) inherits the same pre-segmentation design while the fine segmentation is achieved evolving one whole active surface which intersects and segments all the PET data volume (i.e. all slices) at once. Nevertheless, to initialize such an algorithm a three-dimensional shape is required and the output of the pre-segmentation (step "e1" in Fig. 1B) need to be modified accordingly. To generate a suitable initial shape, we experimented two different approaches: A) the ROI is transformed in an ellipsoid enclosing the SUV_{max} and B) using the boundary surface generated by a 3D region growing initiated at the voxel with SUV_{max}.

Approach "A", henceforth referred to as the "ellipsoid", provides a fast and simple to implement a solution. Additionally, using a regular surface as a starting condition for the active surface helps the stability of the evolution. Nevertheless, the choice of using an ellipsoid, although it follows the major axis of the tumour, seems somewhat arbitrary. This motivated the second approach "B" (henceforth "RG-VOI"), chosen because of its capability of "chasing" the tumour starting from

predefined seed. The difference in performance connected with the choice of the initialization algorithm will be discussed in section 4.

Regardless of the choice, a volume of interest (VOI) is produced and feed to the second block in Fig. 1-B. It is worthy of note that the only requirement for the surface initialization step is that the produced boundary envelops part of the tumour, including the SUV_{max}, but it does not require to possess any fine detail.

2.1. The fully three-dimensional active contour

Block II (Fig. 1B) features the active surface algorithm that performs the fine segmentation. Starting from the model proposed by Lankton et al. [38] where the local active contour method for 3D MR datasets was applied via independent segmentation of the 2D slices, we designed a more powerful and coherent segmentation procedure which achieves the simultaneous segmentation of all slices by evolving a single surface within the corresponding three-dimensional space.

To incorporate SUV in the algorithm as well as formulate it in a fully 3D setting, the contour energy to be minimized for PET image segmentation is defined as:

$$E = \int_S \left(\int_{R_{in}} \chi_l(x,s)(SUV(x) - u_l(s))^2 dx + \int_{R_{out}} \chi_l(x,s)(SUV(x) - v_l(s))^2 dx \right) dS \quad (1)$$

where S denotes the active surface (3D), dS the surface area measure, and s the surface parameter (2D), where x denotes a point within the 3D volume and dx the volume measure, where R_{in} and R_{out} represent the 3D regions inside and outside the surface respectively, where SUV represents the intensity function of the standardized uptake value to be segmented, where FX represents the indicator function of a local neighbourhood around the surface point $S(s)$, and where $u_l(s)$ and $v_l(s)$ denote the local mean SUV intensities within the intersections of this local neighbourhood with the volumes R_{in} and R_{out} inside and outside the surface respectively. We choose these neighbourhoods to be spheres of radius l (in our study $l = 3$ has been determined to provide the best performance using trial and error strategy [33]) centred around each point of the surface S. Note that the function FX) evaluates to 1 in a local neighbourhood around each surface point S(s) and 0 elsewhere, thereby localizing the processing of SUV image information. The shape of the surface S then divides each such local region into interior local points and exterior local points in accordance with the surface's segmentation of the SUV. The local means are specified in terms $S_{I_l}(s)$, $S_{E_l}(s)$, $V_{I_l}(s)$ FX, and $V_{E_l}(s)$ which represent the local sums of SUVs and the volumes of their respective portions of the local neighbourhood FX) inside and outside the curve (within R_{in} and R_{out}). More precisely, the local interior region may be expressed as FX and the local exterior region as FX.

$$u_l(s) = \frac{S_{I_l}(s)}{V_{I_l}(s)}, v_l(s) = \frac{S_{E_l}(s)}{V_{E_l}(s)} \quad (2)$$

$$S_{I_l}(s) = \int_{R_{in}} \chi_l(x,s) SUV(x) dx, S_{E_l}(s) = \int_{R_{out}} \chi_l(x,s) SUV(x) dx \quad (3)$$

$$V_{I_l}(s) = \int_{R_{in}} \chi_l(x,s)\, dx, V_{E_l}(s) = \int_{R_{out}} \chi_l(x,s)\, dx \quad (4)$$

$$\chi_l(x,s) = \begin{cases} 1 & when\ x \in l - ball(C(s)); \\ 0 & otherwise; \end{cases} \quad (5)$$

Summarizing, the 3D surface (i.e. either the ellipsoid or the RG-VOI) obtained by the pre-segmentation step is used as input and evolved to minimize the energy E (equation (1)) and consequently to fit the tumour silhouette.

3. Data

3.1. Clinical studies

To experiment our approach we considered the same patient dataset of our previous work [33] consisting of fifty PET studies (lung, head & neck, and brain cancers). Additionally, to compare the performance of the present algorithm with the capabilities of the slice-by-slice approach we used the same gold standard. Concerning the PET data, no sensitive patient information was accessed. The institutional Hospital Medical Ethics Review Board approved this study protocol and all subjects involved were properly informed and released their written consent.

For FDG PET examinations, patients fasted for 12 h before the scan, and successively were intravenously injected with FDG. The PET/CT study began 60 min after the injection and was executed from the top of the skull to the middle of the thigh with the arms along the body.

For MET PET examinations, patients fasted for 4 h before the scan, and successively were intravenously injected with MET. The PET/CT protocol began 10 min after the injection. The study investigated the only brain region.

3.2. PET/CT acquisition protocol

A Discovery 690 PET/CT scanner with time of flight (General Electric Medical Systems, Milwaukee, WI, USA) was used for acquisitions. The PET protocol included a SCOUT scan at 40 mA, a CT scan at 140 keV and 150 mA (10 s), and 3D PET scans (2.5 min per bed position). PET images were reconstructed using a 3D ordered subset expectation-maximization algorithm. Each PET slice consists of 256 × 256 voxels with a grid spacing of 2.73 mm^3 and thickness of 3.27 mm^3. Consequently, the size of each voxel is 2.73 × 2.73 × 3.27 mm^3. Because of the injected radiotracer, tumours appear as hyperintense regions.

The non-diagnostic CT scan was performed for attenuation correction and anatomic localization of the tumour contextually to PET image acquisition. Each CT slice consists of 512 × 512 voxels with size 1.36 × 1.36 × 3.75 mm^3.

3.3. Gold standard

In PET studies, the only valid ground truth can be obtained using histopathology analysis [39]. Obviously, both chemo and radiotherapy while attaching the tumour modify its shape over time so that the actual gold-standard is impossible to retrieve. Consequently, we refer to manual delineations performed by three clinicians with different expertise (the chief nuclear medicine physician, M.I. author, the chief radiotherapy physician, M.S. author, and an expert radiotherapy physician, G.R. author) as a substitute for ground truth [14]. Since judging which region of a PET image should be included in the tumour volume is a challenging task, manual segmentations performed by different operators are typically different. Therefore, we used the software STAPLES [40] to generate a consolidated reference on every PET slice containing the tumour. Briefly, this software is formulated as an instance of the "expectation maximization". As such, it leverages the statistical properties of a set of input contours to compute the most likely consolidated one. In our case, of course, input consisted of the segmentations performed independently by our three experts. In this way, we obtained the "ground truth" necessary to evaluate the performance of the proposed algorithm concerning different radio-tracers and body districts.

4. Results

4.1. Segmentation results

To assess the performance of our segmentation, ten patients with lung cancer (FDG PET), twenty-five patients with head and neck cancers

(FDG PET), and fifteen patients with brain metastases (MET PET) were considered. The ellipsoid and the RG-VOI initialization methods (see section 2) generated very similar results for the majority of the cases. In 45 cases out of 50, the performance in minimizing the difference between manual and automated BTVs using ellipsoid or RG-VOI changed of only 0.3% in terms of dice similarity coefficient (DSC). Nevertheless, in 5 cases out of 50 the pre-segmentation performed with the 3D region growing mistakenly incorporated adjacent healthy tissues so misleading the subsequent evolution. For this reason, we show only the results obtained using the ellipsoid.

From this initial geometry, the active surface is evolved and allowed to locally expand and shrink within the full 3D vicinity of the tumour until convergence.

As stated in the introduction, to evaluate the quality of the result we compare the gold standards (see section 3.3) with the contours obtained by intersecting the active surface with the planes defined by the PET slices. For each clinical case, we compute a set of performance indicators routinely used in literature; namely sensitivity, positive predictive value (PPV), DSC, Hausdorff distance (HD), and Mahalanobis distance (MHD). These indicators are widely used for shape comparison [39,41,42]. They take cumulatively into account the similarity of the described contours at each slice, therefore providing an evaluation of the similarity of the overall three-dimensional shape to the gold standard (for more details see the appendix).

Finally, the values of these parameters are compared to the corresponding results from previous work, directly available from Ref. [33]. Tables 1–3 summarize the performance for the three lesion datasets, according to the formulas in the appendix.

Table 4 summarizes the results from Tables 1–3 and emphasizes that the 3D segmentation, based on the active surface, performed better than the slice-marching version, overall increasing the DSC of about 2%.

We performed an analysis of the variance (ANOVA) on the DSC to evaluate the similarity of the segmentations obtained from the two methods, across all the 50 cases considered, on a statistical basis. Table 5 compares the results of such analysis. We consider a difference between two segmentations to be "significant" when the p-value is < 0.05. Therefore, the fully 3D approach, with a mean DSC of $88.06 \pm 2.74\%$, not only performed overall better than the old approach (DSC $= 86.47 \pm 3.24\%$), but with p-value ~ 0.0083 provided a significantly different result as well.

The purely numerical evaluation of the results presented here was further supported by feedback provided by our clinical staff. In this perspective, a qualitative evaluation based on the Likert score was carried out. The Likert scale provided a tool to the clinicians to rate the two segmentations with respect to the perceived clinical reliability of the retrieved contour, judged according to their professional expertise. The 3D approach was, in their perception, the best. Despite its qualitative nature, such evaluation let us understand whether the clinician trusted the segmentation provided by the software and which one between the fully 3D and the slice-by-slice marching approach was, in their perception, the best.

The five-point Likert scale ranges from 1 (worst) to 5 (best): 1. Strong worsened compared to the slice-marching MTV; 2. Moderately worsened; 3. Indifferent, neither worsened or enhanced; 4. Moderately enhanced 5. Strongly enhanced.

Our clinical staff, composed of the chief nuclear medicine physician, the chief radiotherapy physician, and an expert radiotherapy physician analysed the tumour segmentation using 2D and 3D methods. Considering their different clinical backgrounds, the physicians were able to jointly provide a careful evaluation for each lesion. In 54% of cases, the MTV definition was enhanced using the fully three-dimensional algorithm shrinking false-positive uptake areas (Likert score = 4–5). In the remaining 46% of cases, 3D MTVs were comparable with 2D MTVs (Likert score = 3). Fig. 3 reports the qualitative comparison between the two methods, considering the three situations mentioned above.

5. Discussion

As introduced before, there are several advantages in including PET imaging in the routine clinical procedures related to cancer diagnosis and treatment. Since MTV identification is a crucial step, it is of no surprise that a significant number of PET segmentation algorithms have been proposed.

In this study, we upgraded our previous system based on active contours and a slice marching approach [27,33], to full 3D. Some aspects are worthy of note.

If, on the one hand, many studies have suggested the combined use of information from PET and CT, on the other hand, morphological information from CT and metabolic information from PET (opportunely converted into SUV images to include functional aspects of the tumour), are not guaranteed to generate the same boundaries. As such, when this asymmetric relation is not taken into account, it can lead to incorrect results, (as shown in Ref. [43]). In the present paper, as we did in Ref. [33], only PET images have been used to extract MTVs while we will investigate CT inclusion in future work.

Moving toward full 3D and using an active surface requires some adaptation of the pre-segmentation algorithm and several engineering solutions may be conceived. What we require to the pre-segmentation step is to produce a rough surface which encloses the SUVmax and reasonably (i.e. with negligible detail) includes the most of the

Table 1
Performance indicators for 10 clinical cases of lung cancer investigated using FDG-PET. The result of the 3D active surface algorithm is compared against the analogous performance of the slice-marching approach. Mean Sensitivity, PPV, DSC, HD, and MHD are reported. Mean value, standard deviation (std), 95% confidence interval (CI) and coefficient of variation (CV) are reported in the bottom section of the table.

Lung Cancer	Slice-marching algorithm					Active surface algorithm				
	Sensitivity [%]	PPV [%]	DSC [%]	HD [voxels]	MHD [voxels]	Sensitivity [%]	PPV [%]	DSC [%]	HD [voxels]	MHD [voxels]
#1	91.60%	81.70%	86.40%	2.49	1.60	93.53%	81.43%	87.06%	1.19	0.81
#2	97.60%	82.80%	89.60%	1.98	1.39	99.47%	81.68%	89.70%	1.63	0.85
#3	98.50%	71.60%	82.90%	2.59	2.09	79.36%	90.73%	84.67%	1.92	0.83
#4	85.00%	85.00%	85.00%	1.08	0.83	98.75%	81.44%	89.27%	0.94	0.30
#5	98.90%	83.20%	90.40%	1.48	0.72	87.25%	96.76%	91.76%	1.34	0.62
#6	88.80%	77.20%	82.60%	1.69	0.84	93.87%	83.15%	88.18%	1.43	0.50
#7	91.00%	73.60%	81.40%	1.14	0.48	85.39%	80.85%	83.06%	1.09	0.86
#8	96.70%	78.40%	86.60%	1.25	0.91	83.18%	91.28%	87.04%	2.03	1.25
#9	94.70%	76.30%	84.50%	2.60	0.67	91.38%	84.46%	87.78%	1.44	0.77
#10	93.50%	76.60%	84.20%	2.38	0.60	97.94%	80.62%	88.44%	1.79	0.51
Mean	**93.63%**	**78.64%**	**85.36%**	**1.87**	**1.01**	**91.01%**	**85.24%**	**87.70%**	**1.48**	**0.73**
± std	±4.55%	±4.41%	±2.94%	±0.62	±0.51	±6.97%	±5.64%	±2.48%	±0.36	±0.26
± CI (95%)	±2.82%	±2.73%	±1.82%	±0.38	±0.32	±4.32%	±3.50%	±1.54%	±0.22	±0.16
± CV	±4.86%	±5.60%	±3.44%	±0.33	±0.51	±7.66%	±6.62%	±2.83%	±0.24	±0.36

Table 2
Mean Sensitivity, PPV, DSC, HD, and MHD for 25 head and neck cancer studies using FDG-PET. The result of the 3D active surface algorithm is compared against the analogous performance of the slice-marching approach. Mean value, standard deviation (std), 95% confidence interval (CI) and coefficient of variation (CV) are reported in the bottom section of the table.

Neck & head Cancer	Slice-marching algorithm					Active surface algorithm				
	Sensitivity [%]	PPV [%]	DSC [%]	HD [voxels]	MHD [voxels]	Sensitivity [%]	PPV [%]	DSC [%]	HD [voxels]	MHD [voxels]
#1	98.70%	81.30%	89.10%	1.46	0.43	85.99%	95.10%	90.31%	1.07	0.58
#2	83.30%	89.70%	86.40%	1.00	0.69	91.67%	84.62%	88.00%	1.03	1.09
#3	89.80%	76.20%	82.40%	1.07	0.74	92.19%	81.94%	86.76%	1.00	0.62
#4	85.50%	94.60%	89.80%	0.85	0.59	87.10%	93.10%	90.00%	0.93	0.61
#5	93.20%	74.80%	83.00%	1.17	0.36	91.53%	87.80%	89.63%	0.88	0.34
#6	96.20%	81.30%	88.10%	1.42	1.41	91.39%	89.42%	90.40%	1.60	0.83
#7	93.90%	89.90%	91.80%	1.19	1.18	89.09%	95.25%	92.07%	2.09	0.75
#8	99.50%	71.80%	83.40%	2.79	0.60	97.59%	73.97%	84.16%	2.41	0.59
#9	96.90%	78.80%	86.90%	2.46	1.37	91.07%	87.80%	89.41%	1.29	0.81
#10	97.50%	77.10%	86.10%	2.59	0.72	84.49%	90.17%	87.24%	2.73	0.75
#11	73.10%	90.50%	80.90%	1.00	0.71	80.30%	82.81%	81.54%	1.41	1.72
#12	99.60%	73.70%	84.70%	1.40	0.69	81.72%	95.63%	88.13%	0.95	0.75
#13	93.80%	73.80%	82.60%	1.03	0.94	75.29%	92.75%	83.12%	1.03	0.84
#14	91.40%	86.50%	88.90%	1.00	0.78	91.43%	86.49%	88.89%	1.21	1.05
#15	88.80%	74.60%	81.10%	2.78	2.28	84.85%	78.45%	81.52%	3.41	1.22
#16	77.60%	84.90%	81.10%	1.07	1.01	98.28%	75.00%	85.07%	0.95	0.72
#17	89.80%	86.30%	88.00%	1.14	0.75	89.80%	91.67%	90.72%	0.90	0.70
#18	91.90%	87.00%	89.40%	0.90	0.81	85.61%	94.96%	90.04%	1.14	0.44
#19	91.40%	80.00%	85.30%	1.37	1.27	91.09%	81.75%	86.17%	1.37	0.73
#20	96.30%	83.90%	89.70%	0.90	1.16	86.67%	92.86%	89.66%	0.90	0.87
#21	97.30%	80.70%	88.20%	1.88	1.98	82.24%	95.34%	88.31%	1.37	1.14
#22	80.80%	95.10%	87.40%	0.94	1.07	96.13%	82.32%	88.69%	0.94	0.78
#23	78.70%	92.50%	85.10%	0.93	1.00	81.63%	90.91%	86.02%	0.75	0.61
#24	93.30%	70.00%	80.00%	1.33	1.52	83.33%	86.21%	84.75%	0.90	1.03
#25	96.60%	84.30%	90.00%	0.99	0.58	91.01%	91.01%	91.01%	1.28	0.86
Mean	**91.00%**	**82.37%**	**85.98%**	**1.39**	**0.99**	**88.06%**	**87.89%**	**87.66%**	**1.34**	**0.82**
± *std*	±7.33%	±7.30%	±3.40%	±0.61	±0.46	±5.60%	±6.40%	±2.95%	±0.65	±0.28
± *CI (95%)*	±2.87%	±2.86%	±1.33%	±0.24	±0.18	±2.20%	±2.51%	±1.16%	±0.26	±0.11
± *CV*	±8.05%	±8.86%	±3.95%	±0.44	±0.47	±6.36%	±7.28%	±3.37%	±0.49	±0.34

Table 3
Mean Sensitivity, PPV, DSC, HD, and MHD for 15 brain cancer studies using MET-PET. The result of the 3D active surface algorithm is compared against the analogous performance of the slice-marching approach. Mean value, standard deviation (std), 95% confidence interval (CI) and coefficient of variation (CV) are reported in the bottom section of the table.

Brain Cancer	Slice-marching algorithm					Active surface algorithm				
	Sensitivity [%]	PPV [%]	DSC [%]	HD [voxels]	MHD [voxels]	Sensitivity [%]	PPV [%]	DSC [%]	HD [voxels]	MHD [voxels]
#1	93.50%	89.90%	91.70%	0.62	1.06	97.06%	87.68%	92.13%	0.66	0.38
#2	90.10%	78.60%	83.90%	1.33	1.14	93.57%	77.29%	84.66%	1.07	0.46
#3	88.40%	82.80%	85.50%	1.54	0.97	96.21%	79.20%	86.88%	0.85	0.51
#4	76.75%	99.18%	86.33%	0.58	0.61	96.48%	82.04%	88.67%	0.55	0.81
#5	86.47%	95.89%	90.83%	0.58	0.56	88.64%	93.22%	90.87%	0.65	0.57
#6	96.20%	75.60%	84.70%	1.91	1.18	86.73%	85.11%	85.91%	1.73	0.65
#7	91.80%	79.50%	85.20%	2.37	1.22	83.18%	89.32%	86.14%	1.67	1.09
#8	94.50%	84.70%	89.40%	0.79	0.85	96.36%	84.77%	90.19%	0.65	0.43
#9	86.80%	83.30%	85.00%	1.24	1.05	99.16%	77.39%	86.93%	1.53	1.09
#10	91.20%	88.70%	90.00%	1.40	0.93	87.19%	93.57%	90.27%	1.50	0.60
#11	91.80%	82.90%	87.10%	1.54	0.71	83.51%	95.82%	89.24%	1.14	0.57
#12	85.20%	97.00%	90.70%	1.38	0.59	93.14%	90.44%	91.77%	1.55	0.67
#13	93.20%	90.30%	91.70%	1.54	1.07	95.29%	90.36%	92.76%	1.57	0.87
#14	93.00%	84.70%	88.70%	1.81	1.72	80.93%	98.88%	89.01%	1.09	1.00
#15	93.60%	85.80%	89.50%	0.65	0.57	96.36%	84.77%	90.19%	0.65	0.43
Mean	**90.17**	**86.60%**	**88.02**	**1.28**	**0.95**	**91.59%**	**87.32%**	**89.04%**	**1.12**	**0.68**
± *std*	±4.89%	±6.89%	±2.75%	±0.54	±0.32	±5.97%	±6.62%	±2.46%	±0.44	±0.24
± *CI (95%)*	±2.47%	±3.49%	±1.39%	±0.28	±0.16	±3.02%	±3.35%	±1.25%	±0.22	±0.12
± *CV*	±5.42%	±7.95%	±3.12%	±0.42	±0.33	±6.52%	±7.58%	±2.77%	±0.39	±0.36

surrounding high uptake tissue; assuming such tissue is part of the lesion. As a base-line requirement, the desired initial surface, once intersected the slice containing the user input, should produce a boundary which does not exceed significantly the contour provided as input. We implemented two solutions: one computationally fast, based on simple geometric considerations but potentially oversimplified (i.e. an ellipsoid following the main axes of the found anomaly), and one tailored to the data (i.e. exploiting a 3D region growing), computationally more involved and potentially leading to a complex initial shape. Since the surface identified during the pre-segmentation step is input to the active surface evolution, it may affect the outcome of the whole segmentation process (Fig. 1b). Therefore, we investigated the robustness of the proposed 3D enhanced method concerning this initialization choice. We obtained strikingly similar results in forty-five

Table 4
Summary of the performance and comparison of Sensitivity, PPV, DSC, HD, and MHD using the 3D active surface algorithm and the slice-marching approach across different anatomical districts.

Cancer	Sensitivity [Mean ± std]	PPV [Mean ± std]	DSC [Mean ± std]	HD [Mean ± std]	MHD [Mean ± std]
Active surface algorithm					
Lung	91.01 ± 6.97%	85.24 ± 5.65%	87.70 ± 2.48%	1.48 ± 0.36	0.73 ± 0.26
Head & Neck	88.06 ± 5.60%	87.89 ± 6.40%	87.66 ± 2.95%	1.34 ± 0.65	0.82 ± 0.28
Brain	91.59 ± 5.97%	87.32 ± 6.62%	89.04 ± 2.46%	1.12 ± 0.44	0.68 ± 0.24
Slice marching algorithm					
Lung	93.63 ± 4.55%	78.64 ± 4.41%	85.36 ± 2.94%	1.87 ± 0.62	1.01 ± 0.51
Head & Neck	91.00 ± 7.33%	82.37 ± 7.30%	85.98 ± 3.40%	1.39 ± 0.61	0.99 ± 0.46
Brain	90.17 ± 4.89%	86.60 ± 6.89%	88.02 ± 2.75%	1.28 ± 0.54	0.95 ± 0.32

Table 5
Analysis of the variance (ANOVA) on the DSC, showing statistical differences between the results from the two segmentation methods.

ANOVA	F value	F critic value	P-value
Active surface algorithm vs Slice-marching algorithm	7.266660788	3.93811108	0.00826835

cases out of fifty. Consequently, the proposed method proved to be robust concerning the initializing surface. This behaviour can be easily understood by considering the intersection of the active surface with one PET slice and realizing that its local evolution naturally considers information from the neighbouring slices. As such, there is no real need to deploy an involved initialization strategy. Nevertheless, in the remaining five cases the MTV based on the ellipsoid initialization largely outperformed the one obtained with the RG-VOI. Upon investigation, it turned out that the region growing algorithm either included healthy tissues with high uptake or excluded relevant anomalous regions. In all such cases, the surface produced by the RG-VOI was clearly anomalous and grew far beyond the reasonable segmentation boundaries provided by the experts, a well-known limitation of the region growing approach. Nevertheless, our baseline requirement was violated by the RG-VOI and this caused the discrepancy in performance. As such, since the ellipsoid provided reasonable and reliable initializations we judged it, despite its simplicity, to be the best solution for the initialization purpose. Notably, the ellipsoid fulfils our baseline requirement by construction.

One additional advantage of the active surface over the slice marching approach is that it does not require any stopping condition [33], as the tumour boundaries are naturally managed in the vertical direction as well (i.e. the direction perpendicular to the PET slices). As a final note, while in our previous work we demonstrated that the slice-by-slice marching approach performed better than several other state-of-the-art methods, the present paper demonstrates the improved performance obtained migrating the whole system into the full 3D. As such we deemed unnecessary a thorough comparison with other methods.

6. Conclusions

In this paper, the semi-automatic segmentation method introduced in previous work, in the context of SUV-PET, has been upgraded and generalized to full 3D. The method furthers our previous work in which segmentation was achieved using a slice by slice marching approach and segmenting each PET slice separately. The present algorithm features instead an active surface, defined in the three-dimensional space, capable of segmenting all PET slices at once. By design, the algorithm reduces the need for manual input to a minimum and produces tumour segmentations that are independent from such initial input, making the result extremely robust and repeatable.

The quantitative validation carried out in this work was not just to test the performance of the model itself, but to see if the migration into 3D yielded a practical benefit. The results have confirmed that such a benefit is indeed achieved in practice and thus warrants the investment a developer would make in revamping an existing 2D slice-by-slice system into the fully 3D system tested in this paper. We have shown that the fully 3D approach not only removes some limitations of our previous work but it also improves the segmentation.

The advancement is confirmed both numerically, in terms of DSC similarity with the gold standard, and visually, as evaluated by three experts using the Likert score. Since, as it is very common, M. D. regard with criticism the results of automatic/semi-automatic segmentations, the latter evaluation reflects how well these experts perceived the quality of the outcome.

Of course, such result also motivates the additional effort required to migrate in full 3D the tissue classification we proposed in Ref. [34,35]

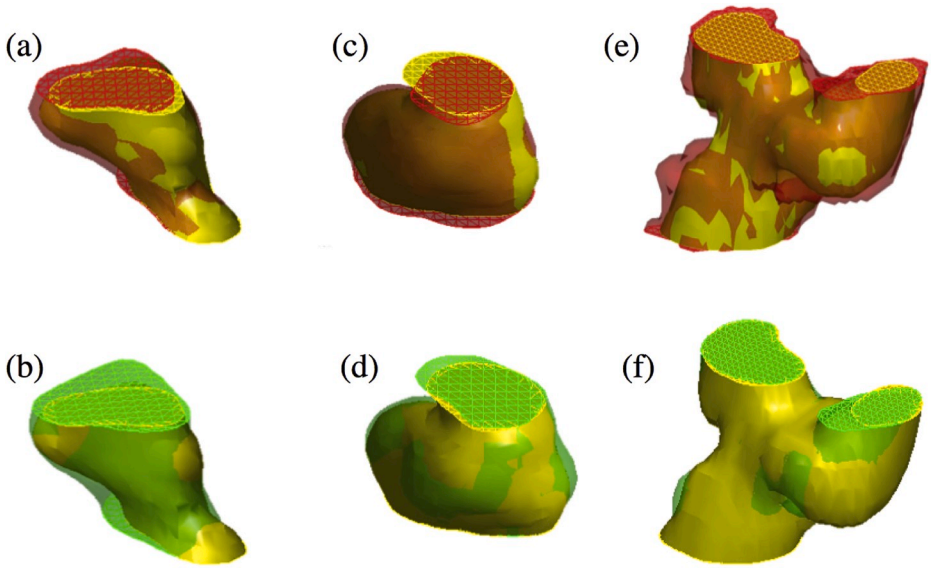

Fig. 3. Three examples showing the difference between the segmentations based on the active surface (proposed approach) and the slice-marching approach [33]. In (a), (c), and (e), segmentations based on slice-marching (red contours) and the gold standards (yellow contours) are superimposed. Surfaces are rendered with a certain degree of transparency to emphasize volume intersections. In the same way, the proposed active surface segmentations (green contours) and the gold standards (yellow contours) are shown in (b), (d), and (f). It is worthy of note that, while gold standard was produced from manual segmentations of all the slices, both the 3D segmentations were obtained starting from the rough manual segmentation on a single slice. (For interpretation of the references to colour in this figure legend, the reader is referred to the Web version of this article).

for the slice-marching approach. Nevertheless, since tissue classification is not yet available in the present algorithm, the inclusion of machine learning components will be reserved to a forthcoming paper. Additionally, in future developments, we may consider the inclusion of information from CT images as well.

Declaration of competing interest

None Declared.

Acknowledgements

All authors declare that they have no conflict of interest. This work was partially supported by grant W911NF-18-1-0281, funded by the USA Army Research Office (ARO): "Extending Accelerated Optimization into the PDE Framework", and by grant R01-HL-143350 funded by the National Institute of Health (NIH) "Quantification of myocardial blood flow using Dynamic PET/CTA fused imagery to determine physiological significance of specific coronary lesions" and by grant FA9550-18-1-0130 funded by the Air Force Office of Scientific Research (AFOSR).

Appendix A

We briefly summarize the meaning of parameters introduced in section 4.1. For a comprehensive description please refer to Ref. [39,41,42].

- Sensitivity, also called true positive volume fraction (TPVF), is the fraction of the total amount of tissue in the retrieved segmentation which overlaps with the reference volume. An ideal segmentation would be 100% sensitive, meaning that all voxels of the reference volume are included in the segmented volume.
- Specificity, also called true negative volume fraction (TNVF), is the fraction of tissue defined in the reference volume that is missed by the segmentation. An ideal segmentation would be 100% specific, meaning that none of the background voxels is included in the segmented volume.
- Positive predictive value (PPV), also called precision, is the fraction of the total amount of tissue in the reference volume which overlaps with the segmented volume.
- Dice similarity coefficient (DSC) measures the spatial overlap between the reference volume and the segmented one. DSC ranges between 0% and 100%, the ideal result being 100%: perfect overlapping.
- Hausdorff distance (HD) is used to measure the most mismatched pair of voxels, one belonging to the boundary of the reference volume and the other belonging to the segmented boundary.
- The Mahalanobis distance (MD) is the correlation of all points belonging to two different points clouds.

References

[1] M. Soret, S.L. Bacharach, I.I. Buvat, Partial-volume effect in PET tumor imaging, J. Nucl. Med. 48 (2007) 932–945, https://doi.org/10.2967/jnumed.106.035774.
[2] R.L. Wahl, H. Jacene, Y. Kasamon, M.A. Lodge, From RECIST to PERCIST: evolving Considerations for PET response criteria in solid tumors, J. Nucl. Med. 50 (Suppl 1) (2009), https://doi.org/10.2967/jnumed.108.057307, 122S–50S.
[3] G.L. Banna, G. Anile, G. Russo, P. Vigneri, M. Castaing, M. Nicolosi, S. Strano, S. Gieri, R. Spina, D. Patanè, G. Calcara, F. Fraggetta, F. Marletta, A. Stefano, M. Ippolito, Predictive and prognostic value of early disease progression by PET evaluation in advanced non-small cell lung cancer, Oncology 92 (2016) 39–47, https://doi.org/10.1159/000448005.
[4] P. Cegla, J. Kazmierska, S. Gwozdz, R. Czepczynski, J. Malicki, W. Cholewinski, Assessment of biological parameters in head and neck cancer based on in vivo distribution of 18F-FDG-FLT-FMISO-PET/CT images, Tumori, 030089161986801, https://doi.org/10.1177/0300891619868012, 2019.
[5] X. Bin, S. Yong, Q.-F. Kong, S. Zhao, G.-Y. Zhang, J.-P. Wu, S.-Q. Chen, W.-D. Zhu, K.-H. Pan, M.-L. Du, M. Chen, Diagnostic performance of PET/CT using 18F-FACBC in prostate cancer: a meta-analysis, Front. Oncol. 9 (2020) 1–9, https://doi.org/10.3389/fonc.2019.01438.
[6] S.M. Bentzen, V. Gregoire, Molecular imaging-based dose painting: a novel paradigm for radiation therapy prescription, Semin. Radiat. Oncol. (2011), https://doi.org/10.1016/j.semradonc.2010.10.001.
[7] M. Niyazi, S. Landrock, A. Elsner, F. Manapov, M. Hacker, C. Belka, U. Ganswindt, Automated biological target volume delineation for radiotherapy treatment planning using FDG-PET/CT, Radiat. Oncol. 8 (2013) 180, https://doi.org/10.1186/1748-717X-8-180.
[8] G. Borasi, G. Russo, F. Alongi, A. Nahum, G.C. Candiano, A. Stefano, M.C. Gilardi, C. Messa, High-intensity focused ultrasound plus concomitant radiotherapy: a new weapon in oncology? J. Ther. Ultrasound. 1 (2013) 6. http://www.jtultrasound.com/content/1/1/6.
[9] A. Comelli, M.C Terranova, L. Scopelliti, S. Salerno, F. Midiri, G. Lo Re, G. Petrucci, S. Vitabile, A kernel support vector machine based technique for Crohn's disease classification in human patients, Conference on Complex, Intelligent, and Software Intensive Systems (2017) 262–273, https://doi.org/10.1007/978-3-319-61566-0_25.
[10] M.L. Belli, M. Mori, S. Broggi, G.M. Cattaneo, V. Bettinardi, I. Dell'Oca, F. Fallanca, P. Passoni, E.G. Vanoli, R. Calandrino, N. Di Muzio, M. Picchio, C. Fiorino, Quantifying the robustness of [18F]FDG-PET/CT radiomic features with respect to tumor delineation in head and neck and pancreatic cancer patients, Phys. Med. 49 (2018) 105–111, https://doi.org/10.1016/j.ejmp.2018.05.013.
[11] A. Comelli, A. Stefano, V. Benfante, G. Russo, Normal and abnormal tissue classification in positron emission tomography oncological studies, Pattern Recogn. Image Anal. 28 (2018) 106–113, https://doi.org/10.1134/S1054661818010054.
[12] A. Stefano, A. Comelli, V. Bravata, S. Barone, I. Daskalovski, G. Savoca, M. G. Sabini, M. Ipplito, G. Russo, A preliminary PET radiomics study of brain metastases using a fully automatic segmentation method, BMC Suppl (2020). Under Second Round Revision.
[13] R. Boellaard, M.J. O'Doherty, W.A. Weber, F.M. Mottaghy, M.N. Lonsdale, S. G. Stroobants, W.J.G. Oyen, J. Kotzerke, O.S. Hoekstra, J. Pruim, P.K. Marsden, K. Tatsch, C.J. Hoekstra, E.P. Visser, B. Arends, F.J. Verzijlbergen, J.M. Zijlstra, E.F. I. Comans, A.A. Lammertsma, A.M. Paans, A.T. Willemsen, T. Beyer, A. Bockisch, C. Schaefer-Prokop, D. Delbeke, R.P. Baum, A. Chiti, B.J. Krause, FDG PET and PET/CT: EANM procedure guidelines for tumour PET imaging: version 1.0, Eur. J. Nucl. Med. Mol. Imag. 37 (2010) 181–200, https://doi.org/10.1007/s00259-009-1297-4.
[14] M. Hatt, B. Laurent, A. Ouahabi, H. Fayad, S. Tan, L. Li, W. Lu, V. Jaouen, C. Tauber, J. Czakon, F. Drapejkowski, W. Dyrka, S. Camarasu-Pop, F. Cervenansky, P. Girard, T. Glatard, M. Kain, Y. Yao, C. Barillot, A. Kirov, D. Visvikis, The first MICCAI challenge on PET tumor segmentation, Med. Image Anal. 44 (2018) 177–195, https://doi.org/10.1016/j.media.2017.12.007.
[15] B. Foster, U. Bagci, A. Mansoor, Z. Xu, D.J. Mollura, A review on segmentation of positron emission tomography images, Comput. Biol. Med. 50 (2014) 76–96, https://doi.org/10.1016/j.compbiomed.2014.04.014.
[16] D. Giambelluca, R. Cannella, F. Vernuccio, A. Comelli, A. Pavone, L. Salvaggio, M. Galia, M. Midiri, R. Lagalla, G. Salvaggio, PI-RADS 3 lesions: role of prostate MRI texture analysis in the identification of prostate cancer, Curr. Probl. Diagn. Radiol. (2019), https://doi.org/10.1067/J.CPRADIOL.2019.10.009.
[17] T. Zhang, L. Guo, K. Li, C. Jing, Y. Yin, D. Zhu, G. Cui, L. Li, T. Liu, Predicting functional cortical ROIs via DTI-derived fiber shape models, Cerebr. Cortex 22 (2012) 854–864, https://doi.org/10.1093/cercor/bhr152.
[18] S. Zhao, Z. Gao, H. Zhang, Y. Xie, J. Luo, D. Ghista, Z. Wei, X. Bi, H. Xiong, C. Xu, S. Li, Robust segmentation of intima-media borders with different morphologies and dynamics during the cardiac cycle, IEEE J. Biomed. Heal. Inf. 22 (2018) 1571–1582, https://doi.org/10.1109/JBHI.2017.2776246.
[19] L. Drever, W. Roa, A. McEwan, D. Robinson, Iterative threshold segmentation for PET target volume delineation, Med. Phys. 34 (2007) 1253–1265, https://doi.org/10.1118/1.2712043.
[20] E. Day, J. Betler, D. Parda, B. Reitz, A. Kirichenko, S. Mohammadi, M. Miften, A region growing method for tumor volume segmentation on PET images for rectal and anal cancer patients, Med. Phys. 36 (2009) 4349–4358, https://doi.org/10.1118/1.3213099.
[21] M. Aristophanous, B.C. Penney, M.K. Martel, C.A. Pelizzari, A Gaussian mixture model for definition of lung tumor volumes in positron emission tomography, Med. Phys. 34 (2007) 4223–4235, https://doi.org/10.1118/1.2791035.
[22] S. Belhassen, H. Zaidi, A novel fuzzy C-means algorithm for unsupervised heterogeneous tumor quantification in PET, Med. Phys. 37 (2010) 1309–1324, https://doi.org/10.1118/1.3301610.
[23] A. Baazaoui, W. Barhoumi, E. Zagrouba, R. Mabrouk, A survey of PET image segmentation: applications in oncology, cardiology and neurology, Curr. Med. Imag. Rev. 12 (2015) 13–27, https://doi.org/10.2174/1573405612666151203204003.
[24] B. Foster, U. Bagci, B. Luna, B. Dey, W. Bishai, S. Jain, Z. Xu, D.J. Mollura, Robust segmentation and accurate target definition for positron emission tomography images using affinity propagation, in: 2013 IEEE 10TH Int. Symp. Biomed. IMAGING, 2013.
[25] W. Ju, D. Xiang, B. Zhang, L. Wang, I. Kopriva, X. Chen, Random walk and graph cut for Co-segmentation of lung tumor on PET-CT images, IEEE Trans. Image Process. 24 (2015) 5854–5867, https://doi.org/10.1109/TIP.2015.2488902.
[26] A. Stefano, S. Vitabile, G. Russo, M. Ippolito, M.G. Sabini, D. Sardina, O. Gambino, R. Pirrone, E. Ardizzone, M.C. Gilardi, An enhanced random walk algorithm for delineation of head and neck cancers in PET studies, Med. Biol. Eng. Comput. 55 (2017) 897–908, https://doi.org/10.1007/s11517-016-1571-0.

[27] S. Lankton, D. Nain, A. Yezzi, A. Tannenbaum, Hybrid geodesic region-based curve evolutions for image segmentation. https://doi.org/10.1117/12.709700, 2007.
[28] T.W. Way, L.M. Hadjiiski, B. Sahiner, H.P. Chan, P.N. Cascade, E.A. Kazerooni, N. Bogot, C. Zhou, Computer-aided diagnosis of pulmonary nodules on CT scans: segmentation and classification using 3D active contours, Med. Phys. (2006), https://doi.org/10.1118/1.2207129.
[29] D. Mendes, N. Ferreira, J. Silva, F. Caramelo, 3D liver segmentation in computed tomography and positron emission tomography exams through active surfaces, in: Proc. - 2015 IEEE 4th Port. Meet. Bioeng. ENBENG 2015, 2015, https://doi.org/10.1109/ENBENG.2015.7088895.
[30] R.G. M, N.A. S, S Hamdy, M.G. M, Automatic liver segmentation from abdominal MRI images using active contours, Int. J. Comput. Appl. (2017), https://doi.org/10.5120/ijca2017915512.
[31] M. Abdoli, R.A.J.O. Dierckx, H. Zaidi, Contourlet-based active contour model for PET image segmentation, Med. Phys. (2013), https://doi.org/10.1118/1.4816296.
[32] M. Zhuang, R.A.J.O. Dierckx, H. Zaidi, Generic and robust method for automatic segmentation of PET images using an active contour model, Med. Phys. 43 (2016) 4483–4494, https://doi.org/10.1118/1.4954844.
[33] A. Comelli, A. Stefano, G. Russo, M.G. Sabini, M. Ippolito, S. Bignardi, G. Petrucci, A. Yezzi, A smart and operator independent system to delineate tumours in Positron Emission Tomography scans, Comput. Biol. Med. 102 (2018) 1–15, https://doi.org/10.1016/j.compbiomed.2018.09.002.
[34] A. Comelli, A. Stefano, G. Russo, S. Bignardi, M.G. Sabini, G. Petrucci, M. Ippolito, A. Yezzi, K-nearest neighbor driving active contours to delineate biological tumor volumes, Eng. Appl. Artif. Intell. 81 (2019) 133–144, https://doi.org/10.1016/j.engappai.2019.02.005.
[35] A. Comelli, A. Stefano, S. Bignardi, G. Russo, M.G. Sabini, M. Ippolito, S. Barone, A. Yezzi, Active contour algorithm with discriminant analysis for delineating tumors in positron emission tomography, Artif. Intell. Med. 94 (2019) 67–78, https://doi.org/10.1016/j.artmed.2019.01.002.
[36] A. Comelli, A. Stefano, A fully automated segmentation system of positron emission tomography studies, in: Annual Conference on Medical Image Understanding and Analysis, 2020, https://doi.org/10.1007/978-3-030-39343-4_30.
[37] A. Comelli, A. Stefano, S. Bignardi, C. Coronnello, G. Russo, M.G. Sabini, M. Ippolito, A. Yezzi, Tissue classification to support local active delineation of brain tumors, in: Annual Conference on Medical Image Understanding and Analysis, 2020, https://doi.org/10.1007/978-3-030-39343-4_1.
[38] S. Lankton, D. Nain, A. Yezzi, A. Tannenbaum, Hybrid geodesic region-based curve evolutions for image segmentation, in: J. Hsieh, M.J. Flynn (Eds.), Med. Imaging 2007 Phys. Med. Imaging, International Society for Optics and Photonics, 2007, 65104U, https://doi.org/10.1117/12.709700.
[39] M. Hatt, J.A. Lee, C.R. Schmidtlein, W. Lu, R. Jeraj, Classi fi cation and evaluation strategies of auto-segmentation approaches for PET : report of AAPM task group No.211, Med. Phys. 44 (2017).
[40] S.K. Warfield, K.H. Zou, W.M. Wells, Simultaneous truth and performance level estimation (STAPLE): an algorithm for the validation of image segmentation, IEEE Trans. Med. Imag. 23 (2004) 903–921, https://doi.org/10.1109/TMI.2004.828354.
[41] J.K. Udupa, V.R. Leblanc, Y. Zhuge, C. Imielinska, H. Schmidt, L.M. Currie, B. E. Hirsch, J. Woodburn, A framework for evaluating image segmentation algorithms, Comput. Med. Imag. Graph. 30 (2006) 75–87, https://doi.org/10.1016/j.compmedimag.2005.12.001.
[42] A.A. Taha, A. Hanbury, Metrics for evaluating 3D medical image segmentation: analysis, selection, and tool, BMC Med. Imag. 15 (2015) 29, https://doi.org/10.1186/s12880-015-0068-x.
[43] A. Stefano, S. Vitabile, G. Russo, M. Ippolito, F. Marletta, C. D'Arrigo, D. D'Urso, M. G. Sabini, O. Gambino, R. Pirrone, E. Ardizzone, M.C. Gilardi, An automatic method for metabolic evaluation of gamma knife treatments. https://doi.org/10.1007/978-3-319-23231-7_52, 2015.

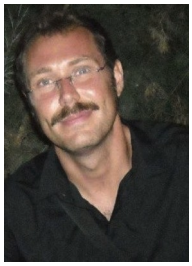

Albert Comelli is a Research/Scientist in Biomedical Image Processing and Analysis at the Ri.MED Foundation. Research Affiliate Long Term at the Laboratory of Computational Computer Vision (LCCV) in the School of Electrical and Computer Engineering at Georgia Institute of Technology, Atlanta, Georgia. He received the PhD in Computer Engineering at the University of Palermo, Combined BSc's/MSc's Degree in Computer Science at the University of Catania. His research interests include medical image processing and medical data analysis.

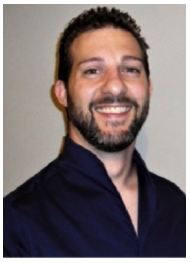

Samuel Bignardi obtained both his M.S. degree in Physics, and his Ph.D. degree in Earth Sciences (Geophysics). Since 2017 he has been working as a Research Scientist in the School of Electrical and Computer Engineering at the Georgia Institute of Technology. His research interests include geophysics, applied physics, active surfaces, medical imaging, and numerical computing.

Alessandro Stefano is a Research Scientist at the Institute of Molecular Bioimaging and Physiology, National Research Council of Cefalu'. He received the Laurea degree (summa cum laude) and the Ph.D. in computer engineering in 2005 and 2016, respectively. His research interests include medical image processing.

Giorgio Russo received the Laurea (summa cum laude) degree in physics (2003), and the medical physics qualification (2007). His research interests include the development of elaboration methods to biomedical imaging.

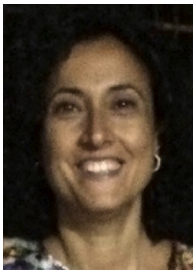

Maria Gabriella Sabini received the Laurea degree in physics in 1997, and the medical physics qualification in 1999. He is currently the head of Medical Physics Unit at Cannizzaro Hospital.

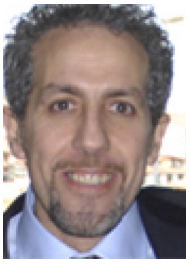

Massimo Ippolito is the head of Department of Nuclear Medicine at Cannizzaro Hospital. He received the Laurea degree (summa cum laude) in medicine and Surgery at the University of Catania in 1992.

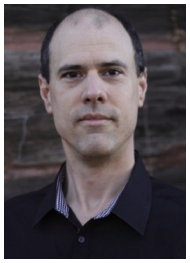

Anthony Yezzi holds the position of Julian Hightower Chair Professor within the School of Electrical and Computer Engineering at Georgia Institute of Technology where he directs the Laboratory for Computational Computer Vision. He has over twenty years of research experience in shape optimization via geometric partial differential equations. He has consulted for a number of companies including GE, 3 M, MZA, Philips, Picker, and VTI.